STUDY OF THE SUITABILITY OF ALUMINUM ALLOYS FOR ADDITIVE MANUFACTURING BY LASER POWDER-BED FUSION

Arnold MAUDUIT[1], Sébastien PILLOT[1], Hervé GRANSAC[1]

After determining the parameters for laser powder-bed fusion, aluminum alloys 2017A, 2219, 7075, 7020, 6061, 5083, 1050A, AlMg14 and AlSi10Mg by using in an experimental design; we were interested in the operating mode of the laser during melting: keyhole mode vs. conduction mode. After determining the operating mode, the maximum temperatures reached during laser melting were calculated theoretically and compared with the evaporation actually observed for certain chemical elements (e.g. Mg and Zn).

The metallurgical quality of the different alloys produced by laser melting was also studied. A hot cracking phenomenon for certain alloys was observed. The explanation of this phenomenon is presented by means of curves of sensitivity to hot cracking. One criterion for implementing aluminum alloys by laser powder-bed fusion is thus possible.

Keywords: laser powder-bed fusion, aluminum alloys (series 2000, 7000, 6000, 5000, Al-Mg, Al-Si), evaporation of chemical elements, hot cracking

1. Introduction

Metal laser powder-bed fusion is an additive manufacturing technique. It is defined by layer-by-layer construction of the desired parts: a laser melts the metal powders following 3D data input into a computer. This process is now well known and well described [1].

After determining the parameters (through experimental design) of implementation by laser melting of aluminum alloys 2017A, 2219, 7075, 7020, 6061, 5083, 1050A, AlMg14 and AlSi10Mg, we are interested initially in the operating mode of the laser (keyhole mode / conduction mode) and in the maximum temperatures reached. Changes in the chemical composition of the aluminum alloys studied is then presented. Secondly, the study is directed towards the cracking phenomena that certain alloys present.

[1] CETIM CERTEC (CRAl : Centre de Référence de l'Aluminium, Pole matériaux et procédés), 9 boulevard Lahitolle, Bourges, France

2. Equipment and methods

2.1. Powder-bed laser melting machine

The machine used in this study is a PHENIX SYSTEMS PM 100 equipped with a 200 W fiber laser YAG (Fig. 1).

Fig. 1. Selective laser melting machine – PHENIX SYSTEMS PM100 – 200 W.

The platform on which parts and samples are built are made of aluminum alloy. The temperature within the processing chamber was set to 200°C. All trials were performed with protective atmosphere (pure Argon - min 99.99%) to prevent oxidation of the aluminum alloys; the layer thickness was set to 30 µm. Manufacturing strategy influences the properties of fabricated parts. Several manufacturing strategies exist, and our choice is known as “crossed” (Fig. 2). In this strategy, tracks built in the same plane all have the same orientation. The execution order of the tracks is shown in Fig. 2 (order of lasing). The direction of the laser beam (and therefore the tracks) alternates. The square in Fig. 2 indicates the direction of manufacturing tracks (first layer with red arrow, followed by the second with green arrow), hence the term “crossed” strategy.

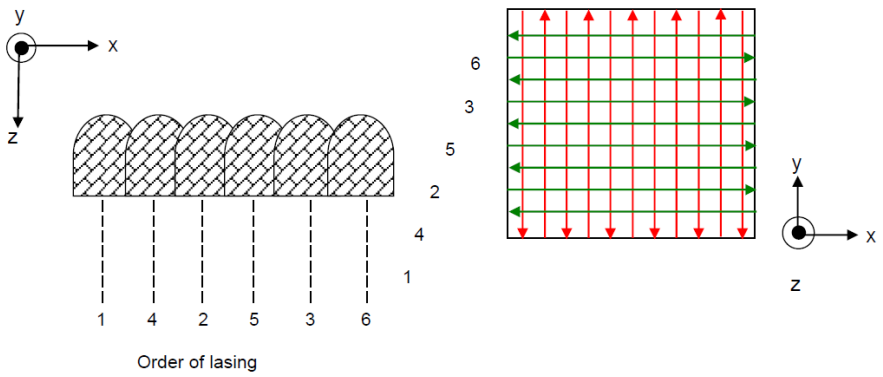

Fig. 2. “Crossed” manufacturing strategy.

2.2. Aluminum alloys – powder – samples

Alloys 2017A, 2219, 7075, 7020, 6061 are structural hardening alloys. They are found in the form of products that are laminated, extruded, drawn or forged. Its main application areas are aeronautics, weapons and general mechanics. Alloy 2219 show good mechanical resistance to heat and proper weldability. Among aluminum alloys, 7075 possesses one of the highest degrees of strength. Alloy 7020 has relatively good mechanical characteristics, as well as proper operational and metallurgical weldability. Alloy 6061 offers a good compromise of properties between average mechanical characteristics, good resistance to corrosion and adequate weldability.

Alloy 5083 is suited for applications requiring good weldability, excellent resistance to corrosion in marine or industrial atmospheres and/or relatively good mechanical characteristics at low temperatures. Alloy 1050A is non-alloyed aluminum, having aluminum content of at least 99.5%. It is one of the most common grades.

The AlSi10Mg alloy is primarily used for molding. For over a decade, this alloy has been used for laser additive manufacturing with varying success: it was among the first to be supplied as powder (industrially) [2]. The AlSi10Mg alloy used in this study was provided by TLS Technik.

Alloy AlMg14 is not marketed like the above. Thus, it has no defined application. A casting of approx. 52 kg was produced at CTIF (centre technique des industries de la fonderie).

These different alloys (except AlSi10Mg) were atomized under argon by the LERMPS laboratory in Belfort.

The characteristics of the powders from the different alloys mentioned above are summarized in Table 1. Note the relatively identical "powder" characteristics for all the alloys.

Table 1

Particle size and morphological characteristics of the powders used.

Alloys	**Powder characteristics**			
	D_{10} (µm)	**D_{50} (µm)**	**D_{90} (µm)**	**Morphology**
2017A	6.3	12.8	22.8	Spherical
2219	5.0	9.8	19.3	Spherical
7075	7.1	12.5	20.3	Spherical
7020	5.7	12.5	24.9	Spherical
6061	9.5	23.1	44.2	Spherical
5083	6.2	13.7	24.6	Spherical
1050A	6.4	14.4	27.9	Spherical
AlMg14	7.6	19.7	39.4	Spherical
AlSi10Mg	9.1	18.4	32.6	Spherical

With D_{xx} is the diameter for which xx% of the number of particles are smaller.

All the test pieces produced and used in the study were cubes measuring 10 mm per side.

2.3. Micrographic examination and SEM

Samples for micrographic evaluation were conventionally prepared (cutting, mounting, polishing, micrographic etching, etc.) prior to observation under an optical microscope, Zeiss imager M2m AXIO. For information purposes, three types of etching were used:

- Reagent with sulfuric acid (10% H_2SO_4 and 5% HF)
- Barker's reagent (electrolytic etching)
- Keller's reagent

Similarly, samples for Scanning Electron Microscopy (SEM) were prepared in the usual fashion and observed under a SEM Zeiss EVD. The latter is equipped with an Energy Dispersive X-ray Spectroscopy (EDS) sensor.

2.4. Chemical analysis by ICP-AES

All the chemical analyses of this study were performed by inductive coupled plasma and atomic emission spectroscopy (ICP-AES).

The measurements of atomic emission spectrometry are performed after mineralization of the powders and solid samples (cube). For this characterization technique, the quantification threshold corresponds to content of 0.005% (by weight). The device used is an optimum 7300 DV.

3. Results and analysis

3.1. Preliminary results

The objective was to determine an optimum SLM processing window for the aluminum alloys. Three main processing parameters (factors for a design of experiment, or DOE) were selected:

- the laser scan velocity, denoted as v
- the recovery rate between two beam paths, Tr, which is directly related to the scan spacing, E_v (being the distance between two consecutive laser beams)
- and the compacting indicator, T_c (the compacting indicator being the percentage of the layer thickness deposited in excess of stated thickness, e.g. a T_c of 50% for a layer of 30 µm gives a deposited powder thickness of 45 µm)

Values too low or too high for these factors lead to decreased densification, and hence poor mechanical properties for the manufactured components.

We could use a Box Behnken DOE to meet our needs – one DOE per material. The output of this DOE is the closed porosity (or internal porosity of the

material). Table 2 summarizes the main parameters of interest for the manufacturing of samples in the aluminum alloys studied.

Table 2

Manufacturing parameters

Alloys	Power (W)	Speed v (m/s)	Coverage indicator Tr (%)	Compacting indicator Tc (%)
2017A	200	0,35	60	50
2219	200	0,6	40	100
7075	200	0,9	60	0
7020	200	0,5	50	0
6061	200	0,6	50	0
1050A	200	0,6	30	0
5083	200	0,6	40	0
AlMg14	200	0,3	60	0
AlSi10Mg	200	0,7	60	50

3.2. Operating mode: conduction mode or keyhole mode

Laser powder-bed fusion in additive manufacturing can operate in two modes: conduction mode or keyhole mode. Laser powder-bed fusion in conduction mode requires lower energy densities and is not unlike "conventional" welding processes (such as electric arc welding). However, laser melting in keyhole mode (also found in other high-energy processes, like electron beam) requires much higher energy densities. According to Knudtson [3], the laser intensity needed to maintain a keyhole is at least 5.10^7 W/cm². In this mode, the energy density is so high it vaporizes the metal found directly under the beam, which creates a keyhole. Capillary walls of molten liquid metal are formed. The molten pool thus created and maintained moves along with the laser beam. Keyhole mode is characterized by depth of penetration, which is shown during manufacture by construction tracks that are deeper than they are wide – unlike conduction mode, where the construction tracks are generally as wide as they are deep (Fig. 3).

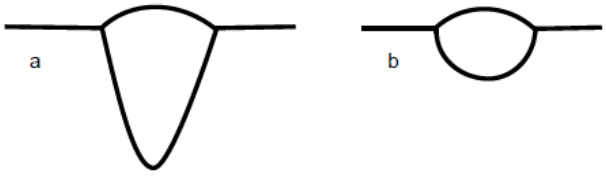

Fig.3. a) Track in keyhole mode – b) Track in conduction mode

In our study, it is interesting to determine the laser melting operating mode. Indeed, this will allow us to apply either conduction or keyhole theories.

3.2.1. Determination of laser intensity

Laser intensity is defined as the power per unit of area in W/cm².

Thus, laser intensity:

$$I_{laser} = \frac{P}{2\pi\sigma^2} \quad (1)$$

With P for power and σ for standard deviation of Gaussian distribution of laser intensity defined as follows:

$$I(r) = I_0 \exp(\frac{r^2}{2\sigma^2}) \quad (2)$$

With r for variable (radius).

As Gaussian distribution is mathematically infinite, it is usual to set a limit radius, r_b, also called conventional radius of the calorific mark, such that this radius defines a limit circle in which the actual existence of the laser intensity can be demonstrated. Conventionally, the limit distance, r_b, is set such that the laser intensity represents 4.55% of the maximum intensity located in the center of the calorific mark.

$$r_b = \sigma\sqrt{6} \quad (3)$$

On the PHENIX SYSTEMS 200 W machine, the diameter, d, of the laser spot at the focal point can be considered 2 times r_b and is defined by:

$$d\ (\mu m) = 2r_b = \frac{197{,}2.\delta}{\pi} \quad (4)$$

With δ for the length of the laser beam (here 1.064 µm)

Thus: $\sigma = \frac{r_b}{\sqrt{6}} = 13{,}6\ \mu m$ and $I_{laser} = 1{,}72.10^7\ W/cm^2 \leq 5.10^7\ W/cm^2$.

The operating mode of powder-bed laser melting is thus by conduction while we are close to the limit holding of the keyhole.

3.2.2. Observation of the construction tracks

As shown above, construction tracks in conduction mode are as wide as they are deep, and do not have a significantly marked depth of penetration (unlike in keyhole mode).

In Fig. 4, we see some tracks of the different alloys studied. They clearly appear to belong to the conduction mode. Additionally, they have an almost hemispherical shape.

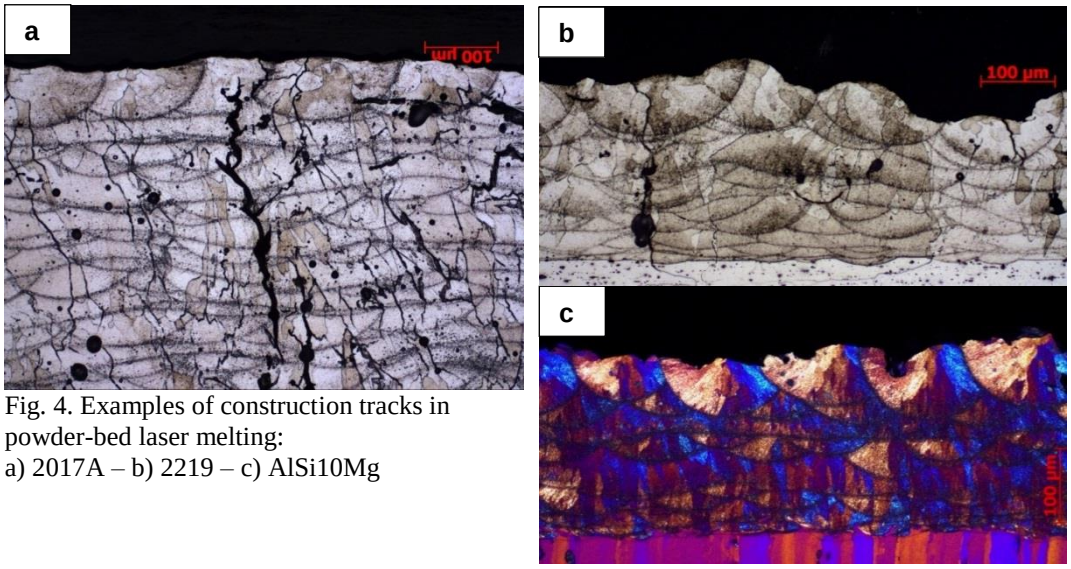

Fig. 4. Examples of construction tracks in powder-bed laser melting:
a) 2017A – b) 2219 – c) AlSi10Mg

3.3. Study of aluminum alloy test pieces obtained by powder-bed laser melting

3.3.1. Evaporation of chemical elements

As we showed in article [2], certain chemical elements having a low evaporation point can vaporize, e.g. magnesium. Our objective is to demonstrate (simply) that the evaporation of certain chemical elements is legitimate. Given that the operating mode is by conduction (3.2.3), thus we can use the laws governing this. According to Tissot [4], to simplify the problem, laser lines are modelled by a hemispherical molten pool, which is close to reality (Fig. 4). The temperature changes corresponding to transfer by pure conduction in the molten pool can be evaluated using Fourier's law [4]. Assuming one-dimensional heat transfer, the power crossing the envelope of the liquid bath can be written as:

$$q = -\lambda\,(2\pi r^2)\,\frac{\Delta T}{r} \tag{5}$$

This entails a temperature variation of:

$$\Delta T = \frac{q}{2\lambda\pi r} \tag{6}$$

- q for power crossing the envelope: $q = A\,P$ with A the absorption coefficient of the laser beam (wavelength 1.064 µm). According to Pierron [5], the absorption coefficient of the beam in conduction mode in liquid state is around 20%. Thus, $q = 40\ W$.
- λ for thermal conductivity (of each of the studied alloys) (Table 3)
- r for the radius of the constructed track: the values obtained during the experimental plans are taken for each of the alloys studied (Table 3)

By accepting that the aluminum alloy considered is completely liquid at the edge of the track (hemispherical envelope) for the liquidus temperature, then the maximum temperature of the melt pool is obtained (track).

Table 3

The maximum temperatures reached for each alloy

Alloy	**Thermal conductivity λ (W/(m.°C))**	**Track radius r (µm)**	**Liquidus (°C)**	**ΔT**	**Maximum temperature (°C)**
2017A	134	82	640	579	1219
2219	134	62	645	766	1411
7075	130	74	635	662	1297
7020	137	94	645	494	1139
6061	153	97	652	429	1081
1050A	229	69	658	403	1061
5083	117	89	638	611	1249
AlMg14	90	150	630	472	1102
AlSi10Mg	103	78	600	792	1392

The maximum temperature reached in the melt pool (track) oscillates between 1061°C and 1411°C, according to the alloy (Table 3); the average is 1233 ±163°C.

Given these temperatures, it appears possible that certain elements with low evaporation points (like Mg) vaporize during laser melting. The elements in the chemical composition of the aluminum alloys concerned are typically Mg (see above) and Zn. The evaporation temperature of Mg is around 1090°C [6] and 907°C for Zn [6]. These two elements are present in certain previously mentioned aluminum alloys (Table 3).

The following Table 4 give the chemical compositions (% by weight) of the previous aluminum alloys before (powder) and after laser melting.

Table 4

Chemical composition

2017A	Si%	Fe%	Cu%	Mn%	Mg%	Cr%	Ni%	Zn%	Ti%
Before	0.56	0.40	4.0	0.57	0.72	0.016	0.009	0.21	0.051
After	0.58	0.50	3.9	0.61	0.48	0.035	0.013	0.07	0.031
7075	Si%	Fe%	Cu%	Mn%	Mg%	Cr%	Ni%	Zn%	Ti%
Before	0.081	0.25	1.4	0.054	2.6	0.18	0.007	5.8	0.034
After	0.11	0.27	1.5	0.057	2.1	0.2	0.007	3.9	0.036
7020	Si%	Fe%	Cu%	Mn%	Mg%	Cr%	Ni%	Zn%	Ti%
Before	0.077	0.29	0.16	0.29	1.3	0.13	0.006	4.3	0.025
After	0.13	0.31	0.17	0.30	1.0	0.14	0.009	3.0	0.024
6061	Si%	Fe%	Cu%	Mn%	Mg%	Cr%	Ni%	Zn%	Ti%
Before	0.57	0.26	0.32	0.032	1.2	0.13	0.008	0.006	0.020
After	0.60	0.26	0.29	0.030	1.0	0.12	0.007	0.005	0.020
5083	Si%	Fe%	Cu%	Mn%	Mg%	Cr%	Ni%	Zn%	Ti%
Before	0.14	0.25	0.032	0.60	3.8	0.086	<0.005	0.043	0.027

After	0.21	0.30	0.035	0.60	2.7	0.084	<0.005	0.031	0.028
AlMg14	Si%	Fe%	Cu%	Mn%	Mg%	Cr%	Ni%	Zn%	Ti%
Before	0.23	0.25	0.008	1.0	13.3	0.25	0.005	0.033	0.1
After	0.34	0.26	0.009	0.99	8.7	0.26	0.006	0.018	0.11
AlSi10Mg	Si%	Fe%	Cu%	Mn%	Mg%	Cr%	Ni%	Zn%	Ti%
Before	10.1	0.19	<0.005	<0.005	0.75	0.007	0.009	0.008	0.014
After	10.6	0.16	<0.005	<0.005	0.32	0.005	0.007	0.008	0.009

Note the systematic reduction in the amount of Mg and Zn (when the alloy contains a significant amount of them) from before laser melting (base powder) to after laser melting, which confirms the evaporation of these elements. It can be seen that the other elements vary only a little or not at all before and after laser melting, except for Si. A slight enrichment in Si is seen for almost all the alloys analyzed.

Alloys 1050A and 2219 were not subject to chemical analysis before and after laser melting because 1050A is not alloyed (only a few impurities of Si and Fe), and 2219 only has Cu as an additional element. Thus for these two alloys, there is little or no variation in the chemical composition before and after laser melting.

Table 5

Reduction in the number of chemical elements

Alloys	2017A	7075	7020	6061	5083	AlMg14	AlSi10Mg
Reduction in amount of Mg (%)	33	19	23	17	29	34	57
Reduction in amount of Zn (%)	-	33	30	-	-	-	-

The chemical element Zn has a more marked tendency to evaporate than Mg (Table 5), Zn has a lower evaporation temperature than Mg. A certain variability appears in the evaporation rate of Mg (Table 5) from 17% (for 6061) to 57% (for AlSi10Mg). This can be related in part to the maximum temperature reached of 1081°C for 6061 against 1392°C for AlSi10Mg (Table 3). Note that even if the evaporation temperature of Mg was not reached for alloy 6061, there is evaporation nevertheless. This suggests that the maximum temperatures reached (Table 3) are slightly underestimated.

There is also a strong similarity between the two alloys 7075 and 7020 regarding the reductions in the amount of Mg and Zn, which can be explained by the fact they belong to the same 7000 series.

The chemical element present in the aluminum alloys studied and having the lowest evaporation temperature after Mg and Zn is Mn, at 2061°C [6]. The change in quantity of Mn (before and after melting) is almost zero (for the alloys containing a significant amount of it); thus, we can conclude that there is no

evaporation of Mn and that the manufacturing temperature of the tracks always stays below 2061°C.

3.3.2. Metallographic study

3.3.2.1. Micrographic examination – Microstructure

Apart from the metallurgical quality (porosities and cracks), it is interesting to observe the microstructure of the alloys manufactured by powder-bed laser melting (Fig. 5).

Alloy	Without etching – porosities and cracks	With etching – tracks and grains
2017A	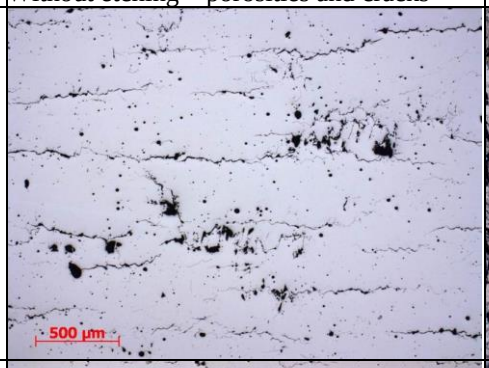	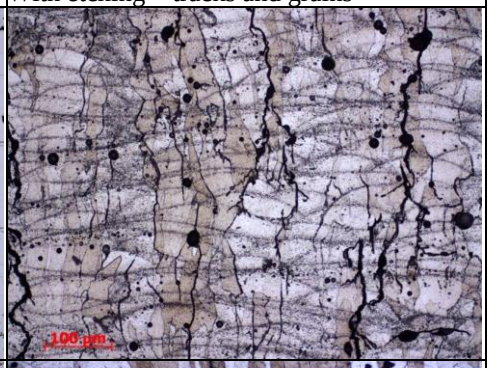
2219	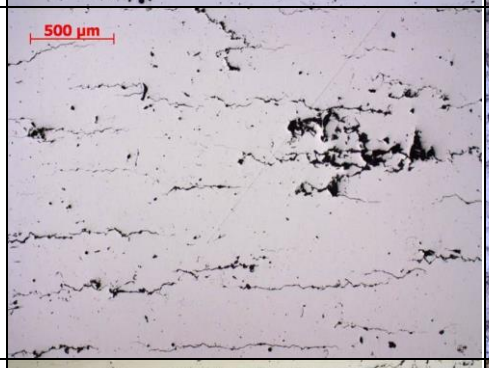	
7075	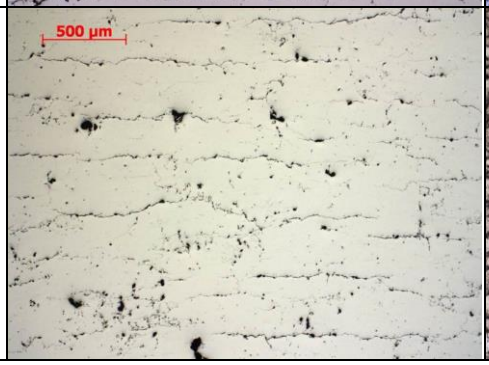	

7020		
6061	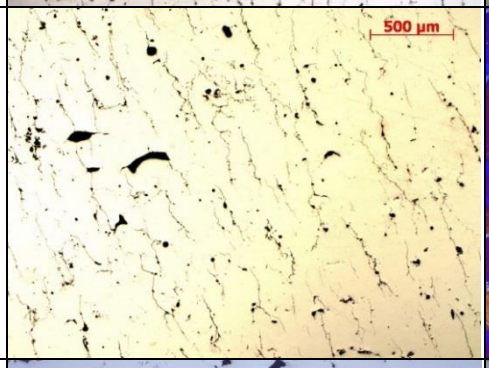	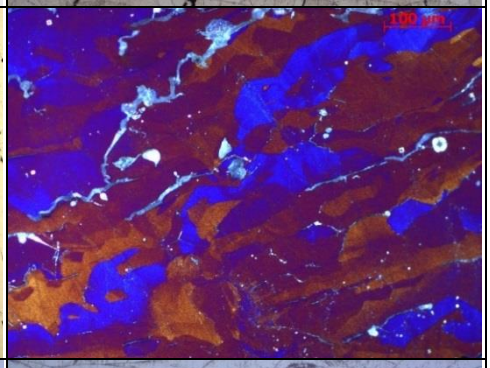
1050A		
5083	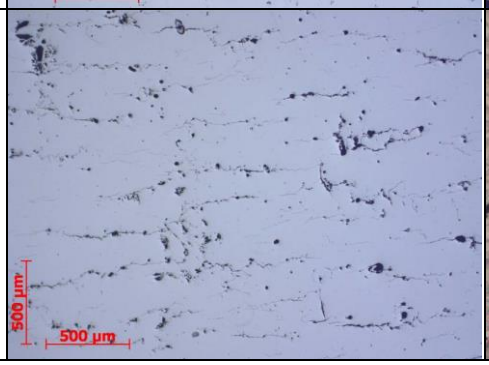	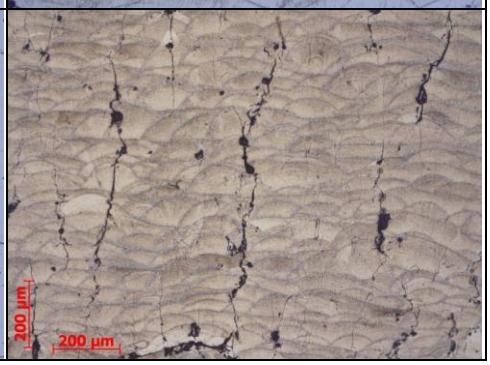

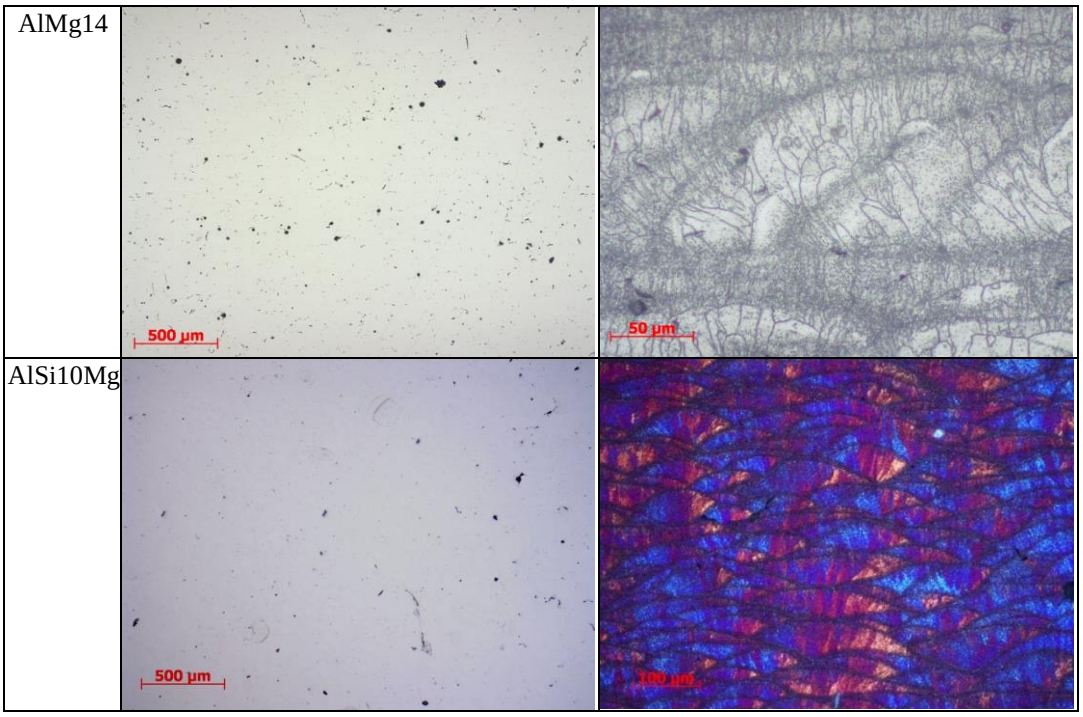

Fig.5. Micrography on as built test piece with and without etching for each alloy studied

The observations (Fig. 5) made on the micrographic sections with and without etching highlight intergranular cracking for alloys 2017A, 2219, 7075, 7020, 6061 and 5083. Only alloys 1050A, AlMg14 and AlSi10Mg do not have cracking. The cracking of alloys 2017A, 2219, 7075, 7020, 6061 and 5083 is similar to hot cracking and more especially to hot cracking during solidification.

Note on the micrographs with etching (Fig. 5) the tracks and orientation of the grain. The construction tracks are visible as "waves", which means that all the micrographic sections are made parallel to the direction of construction of the test pieces, i.e. along the Z axis (Fig. 2).

Inside the tracks, the alloy grains can be distinguished. These develop along paths orthogonal to the isotherms in accordance with the laws of solidification [7]. Thus, the grains are oriented perpendicular to the tangent of the track edges. Once the powders go into liquid state (melt), solidification starts at the molten metal/solid metal interface (this can be a previous manufacture track or the powder bed). The grains of the solid in formation take the orientation of those of the base metal on which they lie. The grains can thus grow from track to track, especially when these are well oriented, i.e. perpendicular to the tangent of the track edges. This phenomenon is more or less visible according to the type of alloy: it is quite marked on wrought alloys (2017A, 7075, 6061, etc.), but much less so on alloys AlSi10Mg and AlMg14.

3.3.2.2. Hot cracking (mechanism)

The conditions for the solidification of construction tracks are high thermal gradients (speed of solidification around 10^5°C/s [2]), strong segregation up to enabling out-of-balance eutectics to form, significant shrinkage, etc. These conditions favor cracking.

The (hot) cracking during solidification occurs in the molten metal in inter-dendritic spaces or at the boundaries of solidification grains, where segregation is particularly significant [7].

Cracking occurs at the end of solidification, when the growing crystals are still separated by inter-dendritic or intergranular liquid. Indeed, at this stage shrinkage becomes significant: strong contractions accompany the transition from liquid to solid, at the moment when – solidification not being completed – films still separate the grains. Not offering any shear resistance, these liquid films, if sufficiently widespread, enable separation of the grains under the effect of the contraction of the metal that is solidifying [7] [8] [9].

SEM observations (Fig. 6) on two alloys studied (2017A and 7075) confirm inter-dendritic cracking. As the speed of solidification is very fast in powder-bed laser melting (around 10^5°C/s), the solid solution dendrites are very fine [2]. However, at high magnification, note that the cracks show stunning groups of well-delineated fine dendrites.

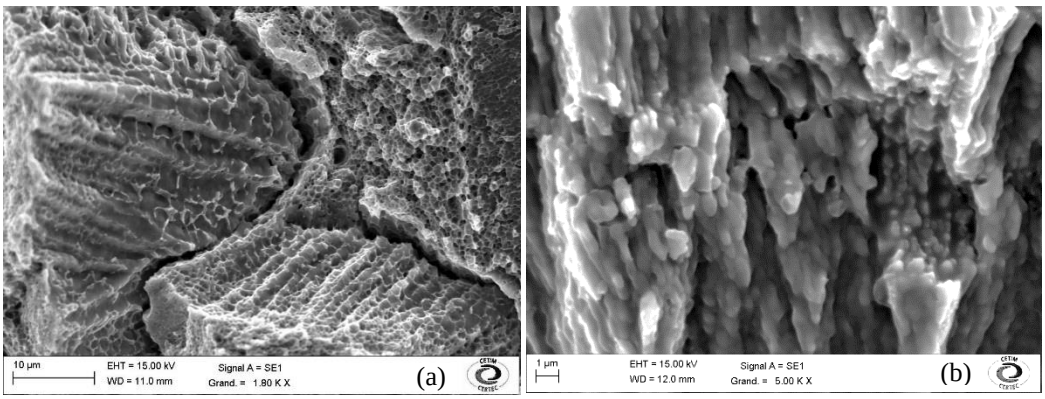

Fig. 6. Observation of solidification crack. a) alloy 2017A – b) alloy 7075.

The main factor in an alloy's sensitivity to hot cracking is its chemical composition. This is how we created the curves of sensitivity to hot cracking for aluminum alloys according to their content of certain chemical elements.

Alloys in the 7000 series with copper, many alloys of the 6000 series and alloys of the 2000 series (with some rare exceptions) are well known for their high sensitivity to hot cracking [7] [8] [9]. Thus, it is not surprising to find this phenomenon (in these alloys), which is confirmed by the curves of sensitivity to

hot cracking given in 3.3.2.3. However, the cracking of 5083 and 2219 remains more surprising.

3.3.2.3. Explanation of hot cracking by curves of sensitivity

In order to discover the zones of the aluminum alloys' maximum sensitivity to hot cracking, the curves of sensitivity were created from different tests, like the Varestraint and Houldcroft tests. Many documents in the literature give these curves, often with an arbitrary scale for the binary alloys, Al-Si, Al-Mg, Al-Cu, etc. (Fig. 7).

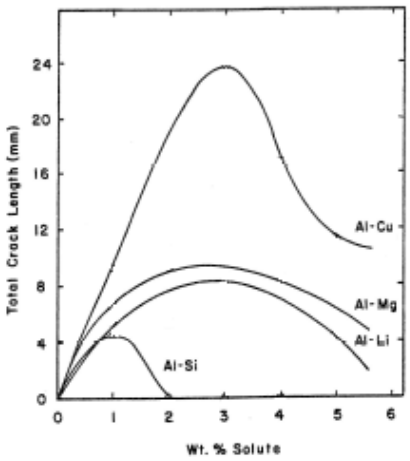

Fig. 7. Experimental results of Varestraint tests for four binary aluminum alloys, according to [9].

However, commercial aluminum alloys are ternary, quaternary, etc., alloys; thus, the idea came about to create curves of sensitivity in three dimensions that more closely represent reality. With these curves of sensitivity, we can explain the hot cracking phenomena for the alloys studied. Fig. 8 gives curves of sensitivity to hot cracking with a common arbitrary scale.

Note here the greater influence of copper on hot cracking. In Fig. 8a, we have shown alloys 2017A, 2219 and 7075 before laser melting (marked (1)) and after laser melting (marked (2)). It can be seen that before and after laser melting these three alloys appear in zones very sensitive to hot cracking. So it is not at all surprising that we find hot cracking in our previous observations (Fig. 5 and 6). Alloy 7075 was also shown in Fig. 8b (Al-Zn-Mg) before and after laser melting (same identification). Again, we see that alloy 7075 appears in a zone sensitive to hot cracking. In the same Fig. 8b, alloy 7020 is noted before and after melting. It appears that this alloy is still found in a zone sensitive to cracking. In Fig. 8c and d, we showed alloys 6061, 5083, AlMg14 and AlSi10Mg. Alloy 6061 is found in a zone of sensitivity to hot cracking (before and after laser melting).

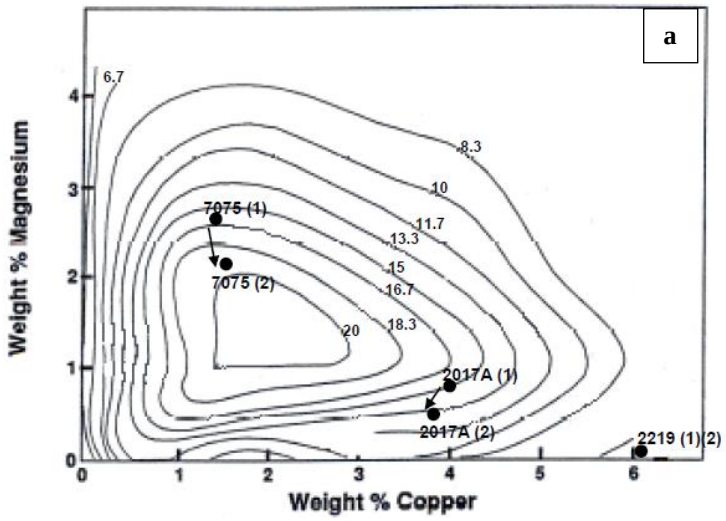
a
Weight % Magnesium
Weight % Copper
6.7
8.3
10
11.7
13.3
15
16.7
18.3
20
7075 (1)
7075 (2)
2017A (1)
2017A (2)
2219 (1) (2)

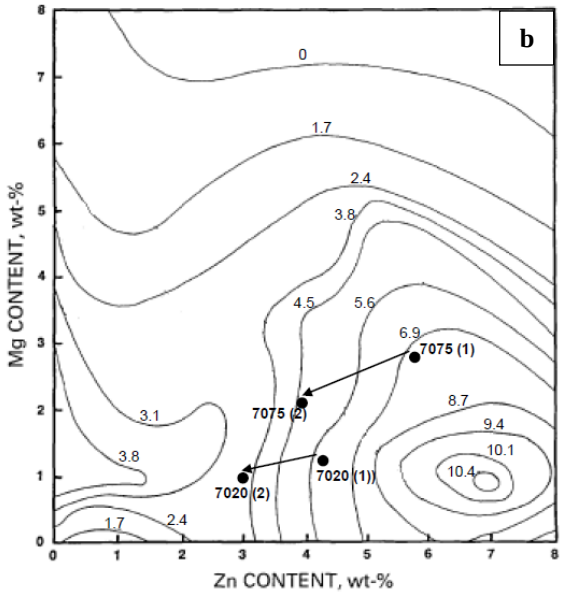
b
Mg CONTENT, wt-%
Zn CONTENT, wt-%
0
1.7
2.4
3.8
4.5
5.6
6.9
7075 (1)
7075 (2)
8.7
9.4
10.1
10.4
3.1
3.8
7020 (2)
7020 (1)
1.7
2.4

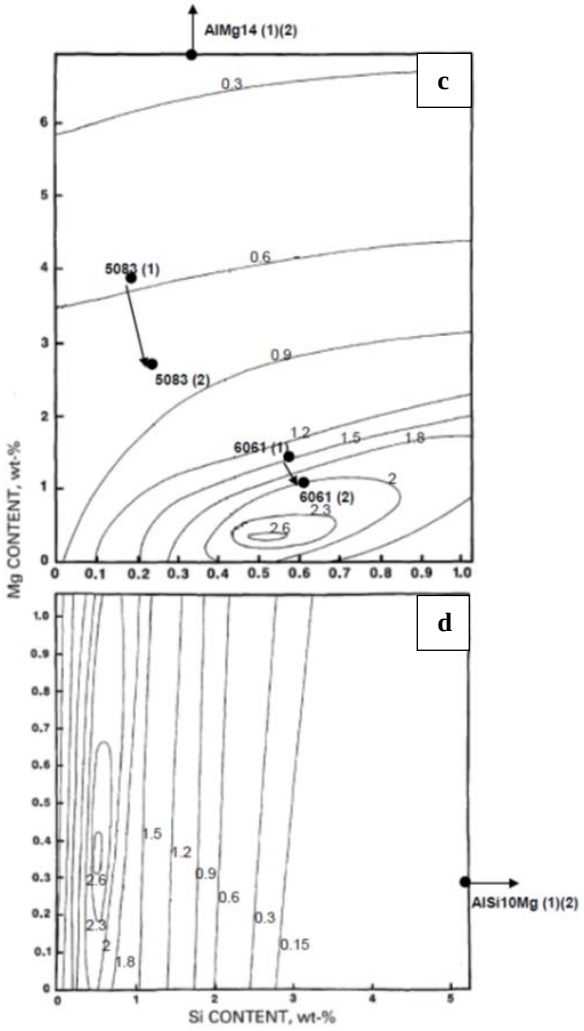

Fig. 8. Curves of sensitivity to hot cracking.
a) Ternary system Al-Cu-Mg, according to [9].
b) Ternary system Al-Zn-Mg, according to [10].
c) and d) Ternary system Al-Si-Mg, according to [10].

Before laser melting, alloy 5083 is found in a zone not highly sensitive to hot cracking. This alloy is known to be weldable (TIG type) without hot cracking, even without filler metal – not the case for alloys of the 6000 series. Given Fig. 8c and the previous remark, we could say that this alloy should not present hot cracking. But after laser melting, the chemical composition of the alloy changes (Table 5), and thus it is found in a zone more sensitive to hot cracking. Alloy

1050A, which is not alloyed, is also known to be weldable (e.g. TIG) without filler metal and does not present hot cracking. Because it has no significant change in its chemical composition, it is effectively free from cracking, as far as we have seen (Fig. 5). The two alloys AlMg14 and AlSi10Mg are located in zones not sensitive to hot cracking both before and after laser melting. And as seen in Fig. 5, these two alloys show no sign of hot cracking. For the AlMg14 alloy, it is the magnesium content of 8.7% (by weight) which avoids the crack (despite an evaporation loss of about 4.6% which has other consequences on the quality of the melt pool). For the AlSi10Mg alloy, it is the very high Si content (10% by weight) which avoids any hot cracking; the other advantage of Si is that it does not evaporate during manufacture.

The curves of sensitivity to hot cracking provide an explanation in all the cases studied in the article whether an alloy will or will not crack.

3.3.2.4. Using the curves of sensitivity to hot cracking on an example from the literature

In the literature there is an interesting example of a 7075 alloy created by laser powder-bed fusion, to which Si was added to confirm improvement in its use [11]. According to Montero Sistiaga [11], alloy 7075 presented a cracking phenomenon identical to that seen in this article (see Fig. 5). Similarly, she observed a change in the chemical composition of 7075 – loss of Mg and Zn. To eliminate the cracks, Montero Sistiaga added 1%, 2%, 3% and finally 4% (by weight) of Si to alloy 7075; she found that the cracking was reduced and disappeared. Alloy 7075, studied by Montero Sistiaga, and these modifications in the chemical composition are shown in Fig. 9 (with alloy 7075 from our study).

We see that alloy 7075 before and after laser melting (marked (1) and (2)) is found in a cracking zone. However, the addition of Si moves the alloy to a zone not sensitive to hot cracking. Thus, alloy 7075 with 3% and 4% Si added is found in a zone not sensitive to hot cracking so that we should not see hot cracking (e.g. on micrographic section). This is exactly what Montero Sistiaga observed in her study: no crack for alloy 7075 with 3% and 4% Si added (while additions of 1% and 2% still showed cracking).

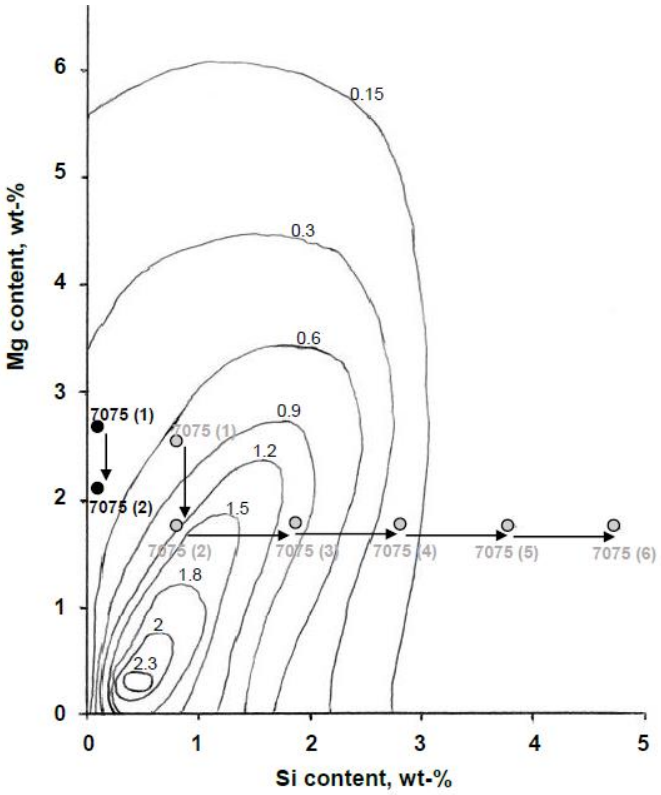

Fig. 9. Curves of sensitivity to hot cracking of the ternary system Al-Si-Mg, according to [12]. Alloy 7075 of our study, black; Alloy 7075 according to [11], grey. 7075(3) addition of 1% Si – 7075 (4) addition of 2% Si – 7075 (5) addition of 3% Si – 7075 (6) addition of 4% Si.

4. Conclusion

It appears that the main operating mode of powder-bed laser melting is conduction mode, meaning that the laws of conduction apply. This then enabled calculation of the theoretical maximum temperatures reached during laser melting. These temperatures explain the change in the chemical composition of the different alloys studied. The theoretical maximum temperatures reached are 1061°C to 1411°C, and it is certain that they do not exceed 2061°C (evaporation temperature of Mn). The chemical elements that evaporate are mainly Mg and Zn because they have the lowest evaporation temperatures. The aluminum alloys contain no other chemical elements that can be affected by this evaporation phenomenon, except lithium, which has an evaporation temperature of 1342°C [6]. We also note that evaporation of the chemical elements is harmful to the metallurgical quality of the test pieces produced by laser melting. According to Herzog [13], evaporation of the volatile elements (like Zn) leads to turbulent molten pools, splatter and porosities. Thus, it is best to avoid aluminum alloys too

charged with magnesium, zinc and possibly lithium for good metallurgical quality of parts produced by laser powder-bed fusion. Moreover, these elements clog the filters of additive manufacturing machines, and of course they represent financial losses.

Certain aluminum alloys show cracking when used in laser melting. This cracking is comparable to the hot cracking during solidification that is found in fusion welding. This cracking is explained and predicted by already available curves of sensitivity to hot cracking. Thus, an important criterion for using aluminum alloys in additive manufacturing by laser powder-bed fusion is hot cracking. Alloys sensitive to this phenomenon cannot be used in this process.

Acknowledgements

The authors thank CETIM (Centre Technique des Industries de la Mécanique) for the funding and support provided for this study.

R E F E R E N C E S

[1]. *Sébastien Pillot*, Technique de l'ingénieur BM7900, Fusion laser sélective de lit de poudres métalliques.

[2]. *Arnold Mauduit, Sébastien Pillot, François Frascati*, Application study of alloy AlSi10Mg by selective laser melting: physical and mechanical properties, microstructure, heat treatments and manufacturing of aluminium metallic matrix composite (MMC). Metallurgical research and technology, 2015,112, 605.

[3]. *J.T. Knudtson, W.B. Green, D.G. Sutton*, The UV-visible spectroscopy of laser produced aluminium plasmas. Appl. Phys. 1987, 61(10), pp. 4771-4780.

[4]. *François Xavier Tissot*. Etude phénoménologique et modélisation du comportement du bain de fusion en soudage TIG en vue d'une application au contrôle du procédé. Rapport CEA. Saclay, 1998, 184p.

[5]. *N. Pierron, P. Sallamand, S. Matteî*, Study of magnesium and aluminium alloys absorption coefficient during Nd-YAG laser interaction. Applied Surface Science, 2007, 253, pp. 3208-3214.

[6]. *D.R. Lide*, CRC Handbook of chemistry and physics, CRC press inc, 2009, 90^{e} ed, 2804 p.

[7]. *C. Boucher*, L'aluminium et ses alliages – soudabilité – métallurgie du soudage. Publications du soudage et de ses applications, 2000, 204 p.

[8]. *G. Mathers*, The welding of aluminium and its alloys. *CRC press* – Woodhead publishing limited, 2002, 242p.

[9]. *C.E. Cross, D.L. Olson, S. Liu*, Aluminium welding. Handbook of aluminium, volume 1, TOTTEN and MAC KENZIE, 2003, pp. 481-532.

[10]. *M.G. Moussavi, C.E. Cross, O. Grong, M. Havl*, Controlling weld metal dilution for optimized weld performance in aluminium. Science and technology of welding and joining, 1997, vol. 2, n°6, pp. 275-278.

[11]. *M.L. Montero Sistiaga, R. Mertensb, B. Vranckena, X. Wanga, B. Van Hoorewederb, J.P. Kruthb, J. Van Humbeeckaa*, Changing the alloy composition of Al7075 for better processability by selective laser melting. Journal of Materials Processing Technology, 2016, 238, pp. 437-445.

[12]. *N. Coniglio, C.E. Cross, T. Michael, M. Lammers*, Defining a critical weld dilution to avoid solidification cracking in aluminum. *Welding research*, 2008, vol. 87, pp. 237-247.
[13]. *D. Herzog, V. Seyda, E. Wycisk, C. Emmelmann*, Additive manufacturing of metals. Acta Materialia, 2016, 117, pp. 371-392.